



Intermetallic solid solution $\text{Fe}_{1-x}\text{Co}_x\text{Ga}_3$: Synthesis, structure, NQR study and electronic band structure calculations

V.Yu. Verchenko^a, M.S. Likhanov^a, M.A. Kirsanova^a, A.A. Gippius^{b,c}, A.V. Tkachev^{b,c}, N.E. Gervits^{b,c}, A.V. Galeeva^b, N. Büttgen^d, W. Krätschmer^d, C.S. Lue^e, K.S. Okhotnikov^f, A.V. Shevelkov^{a,*}

^a Department of Chemistry, Lomonosov Moscow State University, Moscow 119991, Russia

^b Faculty of Physics, Lomonosov Moscow State University, Moscow 119991, Russia

^c A.V. Shubnikov Institute of Crystallography, Moscow 119333, Russia

^d Institut für Physik, University of Augsburg, Augsburg D-86135, Germany

^e Department of Physics, National Cheng Kung University, Tainan 70101, Taiwan

^f Materials and Environmental Chemistry, Stockholm University, Stockholm, Sweden

ARTICLE INFO

Article history:

Received 3 May 2012

Received in revised form

24 May 2012

Accepted 26 May 2012

Available online 4 June 2012

Keywords:

Intermetallics

Iron

Cobalt

Nuclear quadrupole resonance

Solid solution

Crystal and electronic structure

ABSTRACT

Unlimited solid solution $\text{Fe}_{1-x}\text{Co}_x\text{Ga}_3$ was prepared from Ga flux. Its crystal structure was refined for $\text{Fe}_{0.5}\text{Co}_{0.5}\text{Ga}_3$ ($P4_2/mnm$, $a=6.2436(9)$, $c=6.4654(13)$, $Z=4$) and showed no ordering of the metal atoms. A combination of the electronic band structure calculations within the density functional theory (DFT) approach and $^{69,71}\text{Ga}$ nuclear quadrupole resonance (NQR) spectroscopy clearly shows that the Fe–Fe and Co–Co dumbbells are preferred to the Fe–Co dumbbells in the crystals structure. The band structure features a band gap of about 0.4 eV, with the Fermi level crossing peaks of a substantial density of electronic states above the gap for $x > 0$. The solid solution is metallic for $x > 0.025$. The study of the nuclear spin–lattice relaxation shows that the rate of the relaxation, $1/T_1$, is very sensitive to the Co concentration and correlates well with the square of the density of states at the Fermi level, $N^2(E_F)$.

© 2012 Elsevier Inc. All rights reserved.

1. Introduction

The overwhelming majority of intermetallic compounds behave as metals, and exceptions are rare. There exist a number of binary and ternary compounds that are semiconductors. They include several Heusler and half-Heusler compounds [1,2], RuAl_2 and RuGa_2 with the TiSi_2 structure type [3], and FeGa_3 [4]. In 2002, the latter was reported by Häussermann et al. to be an intermetallic semiconductor with the band gap of approximately 0.3 eV [4]. This affirmation was predicted by band structure calculations and proved by resistivity measurements carried out on a FeGa_3 single crystal. Opening of the narrow band gap in the case of FeGa_3 originates from the overlap of the Fe 3d and Ga 4p orbitals; thus, one can expect the same behavior in another intermetallic compounds containing both d and p metals. Transport properties of compounds with the FeGa_3 type of crystal structure, namely CoGa_3 , RuGa_3 , and RuIn_3 , were investigated. As follows from the results of measurements, RuGa_3 [4] and RuIn_3 [5] show semiconductor-like behavior whereas CoGa_3 [4] is a

metallic conductor. This indicates that not only a combination of elements leads to the formation of semiconductor properties but there is another crucial term, which is the number of valence electrons. For the compounds with 17 electrons per formula unit, namely FeGa_3 , RuGa_3 and RuIn_3 , band structure calculations confirm that the Fermi level locates in the band gap whereas for the 18 electron compounds the Fermi level shifts towards the conduction band, dividing nonbonding and antibonding states.

Recently FeGa_3 attracted attention as a potential thermoelectric material [6] and as a candidate for half-metallic ferromagnetism relevant for spintronic applications [7]. It was shown [7] that a few percent cobalt doping to intermetallic FeGa_3 drastically changes properties of the parent compound. Namely, the 5% Co doped specimen reveals itself as a bad metal and a Curie–Weiss paramagnet in contrast to semiconducting and nonmagnetic FeGa_3 . Actually, the observed effect of doping on physical properties is connected with the creation of local magnetic moments and increase of valence electron concentration (VEC) in the parent compound. It appears from this that the number of valence electrons has an impact on transport and magnetic properties, and the substitution of Fe atoms by Co ones to a greater extent demands further investigation. Since both intermetallics FeGa_3 and CoGa_3 possess the same type of crystal

* Corresponding author. Fax: +7 495 939 4788.

E-mail address: shev@inorg.chem.msu.ru (A.V. Shevelkov).

structure we assumed the formation of the continuous solid solution between them. The solid solution with the formula $\text{Fe}_{1-x}\text{Co}_x\text{Ga}_3$ would have an intermediate and controllable number of valence electrons, providing possibilities to study physical properties for different values of VEC. Besides the dependence of physical properties upon VEC, there is another crucial issue, which is the detailed characterization of the solid solution crystal structure depending on the content of cobalt. This issue includes the determination of interatomic distances and angles, and analysis of Fe and Co atoms crystallographic distribution. To this end, local features of the crystal and electronic structure can be probed by nuclear quadrupole resonance (NQR) spectroscopy, which is also proved to be a powerful tool for studying the distribution of electron density through measuring the rate of spin–lattice relaxation [8].

In this work we report on the synthesis, structure, and properties of the $\text{Fe}_{1-x}\text{Co}_x\text{Ga}_3$ solid solution for $0 < x < 1$. In particular, we report on the crystal growth from Ga excess and on the non-Vegard behavior of this solid solution, present evidence on the metal atoms distribution obtained from a combination of the XRD and NQR study, discuss the evolution of its electronic structure with changing Co concentration, and present electrical conductivity for different x values.

2. Experimental section

2.1. Synthesis

The target solid solution $\text{Fe}_{1-x}\text{Co}_x\text{Ga}_3$ was prepared from the elements: Fe powder (Acros Organics, 99%), Co powder (Alfa Aesar, 99.8%), and Ga rods (Aldrich, 99.999%). A series of $\text{Fe}_{1-x}\text{Co}_x\text{Ga}_3$ specimens with $x=0, 0.025, 0.125, 0.25, 0.375, 0.44, 0.5, 0.56, 0.625, 0.75, 0.875, 1$ was synthesized. At first a thin layer of carbon was deposited on the inside of quartz ampoules by pyrolysis of acetone. Reactants with excess gallium (molar ratio $M:\text{Ga}=1:15$, where M is the total quantity of Fe and Co, were loaded into the precarbonized ampoules, which were then sealed under vacuum at a pressure less than 10^{-2} Torr and placed into a programmable furnace. All samples were heated to 1123 K at the rate of 100 K/h, held at this temperature for 55 h to obtain a homogeneous melt, slowly cooled to 793 K at the rate of 4 K/h, and finally cooled to the ambient temperature in the shut off furnace. Excess of gallium metal was separated at 313 K in an Eppendorf 5804R centrifuge, yielding well-shaped silvery-gray crystals with a linear size up to 5 mm. The obtained crystals were purged from the remainder of Ga metal with diluted 0.5 M HCl and washed with distilled water and acetone.

2.2. X-ray diffraction

X-ray powder diffraction experiments were performed on a Stoe STADI-IP diffractometer with $\text{CuK}\alpha_1$ radiation (Ge monochromator, $\lambda_{\text{Cu}}=1.540598 \text{ \AA}$) by using Si as an internal standard ($a=5.43088 \text{ \AA}$). The crystals were finely ground and spread on a thick amorphous film. Unit cell parameters were calculated from least-squares fits using the standard program package Stoe WinXPOW.

For the crystal structure determination, a suitable single crystal with composition $\text{Fe}_{0.5}\text{Co}_{0.5}\text{Ga}_3$, which was confirmed by EDXS, was selected from the products of the synthesis and mounted on an IPDS II diffractometer (Stoe) equipped with a graphite monochromator, a Mo X-ray source ($\lambda_{\text{Mo}}=0.71073 \text{ \AA}$), and an image plate detector. The data collection nominally covered a full sphere of the reciprocal space. The data were corrected for Lorentzian polarization, extinction, and absorption

(assuming a spherical crystal). The crystal structure was solved and refined against F^2 by using SHELX-97 programs. [9]. Details of the data collection and refinement are listed in Table 1. The crystal structure was solved and refined in the space group $P4_2/mmm$, pertinent to the FeGa_3 structure type and confirmed by the systematic extinction conditions. The refined atomic parameters are listed in Tables 2 and 3. As iron and cobalt atoms are not distinguishable by X-ray diffraction, the unique atomic position occupied by the metal atom was introduced as jointly populated by Fe and Co in a 1:1 ratio. Further details on the crystal structure investigation may be obtained from the Fachinformationszentrum Karlsruhe, D-76344 Eggenstein-Leopoldshafen, Germany (fax: +(49)7247-808-666; e-mail: crysdata@fiz-karlsruhe.de), reference number CSD-XXXXXX.

2.3. EDXS analysis

To determine the composition of the obtained samples, crystals were carefully crushed in an agate mortar. After this, fresh chips were investigated with a JSM JEOL scanning electron microscope operated at 30 kV and equipped with an EDX detection system INCA x-Sight. The data were collected from 10 points for each sample and then averaged. In all cases, pure elemental Co was used as a standard.

2.4. Thermal analysis

Simultaneous thermal analysis was performed using an STA 409 PC Luxx (Netzsch) thermobalance. The analysis was performed in dry argon flow up to 1273 K with a heating and cooling rate of 10 K min^{-1} and in air up to 1173 K with the same ramp

Table 1
X-ray single-crystal data collection and refinement parameters for $\text{Fe}_{0.5}\text{Co}_{0.5}\text{Ga}_3$.

Crystal system	Tetragonal
Space group	$P4_2/mmm$
Personal symbol	$tP16$
a [Å]	6.2436 (9)
c [Å]	6.4654 (13)
V [Å ³]	252.04 (12)
Z	4
ρ_{calcd} [g cm ⁻³]	7.025
μ [mm ⁻¹]	37.38
$F(000)$	478
Max. 2θ [°]	58.19
hkl indices range	$-8 \leq h \leq 8$ $-7 \leq k \leq 8$ $-7 \leq l \leq 8$
Independent reflections	204
Reflections with $F_0 > 4\sigma(F_0)$	192
Parameters	15
Goodness-of-fit	1.20
$R^1 [F_0 > 4\sigma(F_0)]$	0.047
R^1/wR^2 (all)	0.051/0.122
Extinction coefficient	0.011 (4)

Table 2
Atomic parameters for the crystal structure of $\text{Fe}_{0.5}\text{Co}_{0.5}\text{Ga}_3$.

Atom	Wyckoff site	x	y	z	s.o.f.	U_{eq} [$\times 10^4 \text{ \AA}^2$]
M	$4f$	0.84566 (17)	$-x$	0	0.5Fe+0.5Co	77 (5)
Ga1	$4c$	0.5	0	0	1	177 (6)
Ga2	$8j$	0.15287 (15)	x	0.24366 (15)	1	163 (5)

Table 3Interatomic distances [Å] for FeGa₃, Fe_{0.5}Co_{0.5}Ga₃, and CoGa₃.

		FeGa ₃ [4]	Fe _{0.5} Co _{0.5} Ga ₃	CoGa ₃ [11]
M	–Ga1 × 2	2.365	2.3635 (6)	2.360
	–Ga2 × 2	2.393	2.3759 (16)	2.368
	–Ga2 × 4	2.500	2.4821 (13)	2.474
	–M	2.769	2.726 (3)	2.710
Ga1	–M × 2	2.365	2.3635 (6)	2.360
	–Ga2 × 4	2.835	2.8443 (8)	2.844
	–Ga2 × 4	2.924	2.8906 (7)	2.877
Ga2	–M	2.393	2.3759 (16)	2.368
	–M × 4	2.500	2.4821 (13)	2.474
	–Ga2	2.756	2.700 (3)	2.679
	–Ga1 × 2	2.835	2.8443 (8)	2.844
	–Ga1 × 2	2.924	2.8906 (7)	2.877

rate. The Proteus Thermal Analysis program (Netzsch) was used for data processing and analyzing.

2.5. Ab-initio calculations

DFT calculations with Full-potential linearized augmented plane wave (FP-LAPW) basis were carried out using the Wien2k package [10]. Muffin-tin spheres radius were ~ 2.3 and ~ 2.0 a.u. for Fe/Co and Ga, respectively, and were slightly adjusted for different types of calculations. Core states were separated with an energy of -8.0 Ry to include the 3s state of Fe/Co and 3p state of Ga into valence states.

Six crystal structures were used for the calculations with $x=0, 0.25, 0.5$ (2 configurations), 0.75 , and 1 . For all of them the calculations were done in several steps in the same way. First of all, position optimization calculations were performed, for which unit cell parameters and initial atomic positions were taken from the literature for FeGa₃ and CoGa₃ [4,11]. For mixed compositions unit cell parameters and atomic coordinates were interpolated. The next step was volume optimization calculations. The 3×3 matrices with different a and c unit cell parameters were calculated (with the position optimization) to obtain the energy of each $\{a, c\}$ configuration. This data were fitted with the second-order polynomial, and positions of the minimum energy cell dimensions $\{a_{min}, c_{min}\}$ were used in composition properties calculations.

The optimization steps were carried out with $R_{min}K_{max}=7.0$ and 1000 k -points in the Brillouin zone. Some extra calculations were done to get optimal basis parameters for composition properties calculations, including the electric field gradient (EFG) and density of states (DOS). The optimal parameters of $R_{min}K_{max}=8.0$ and 2000 k -points were used to obtain properties for different compositions.

2.6. Electrical resistivity measurements

Electrical resistivity was measured in the range of $4.2 \text{ K} \leq T \leq 293 \text{ K}$ by employing a home-built 4-probe dc device. Crystals with a typical size of $4 \times 3 \times 1.5 \text{ mm}^3$ with different Co concentration ($x=0.025, 0.125, 0.5, 0.625$, and 0.75) were selected for the measurements. Current–voltage (I – V) characteristics were taken before the temperature sweeps to make sure that the measurements were performed in the ohmic regime when V is linear with I .

2.7. NQR spectroscopy

The $^{69,71}\text{Ga}$ NQR measurements were performed at $T=15 \text{ K}$ utilizing the home-built phase coherent pulsed NQR spectrometer

with the wide-band solid state NMR probe inserted into closed-cycle cryogen free refrigerator Janis CCS-550. The $^{69,71}\text{Ga}$ NQR spectra were measured using a frequency step point-by-point spin–echo technique. At each frequency point the area under spin–echo magnitude was integrated in the time domain and averaged over scan accumulation number, which depends on the sample. Nuclear spin–lattice relaxation rate was measured using the “saturation recovery” method. Nuclear magnetization recovery curves $M(\tau)$ were obtained from the recovery of the spin–echo intensity as a function of the time interval τ between the saturation pulse comb and the $\pi/2$ – π spin–echo sequence.

3. Results and discussion

3.1. Synthesis and characterization of the samples

In all cases, synthesis was performed by a flux method in excess of liquid gallium [12] and yielded well-shaped silvery-gray crystals of a different shape with linear size up to 5 mm (Fig. 1). The crystals are stable in moist air for months. Heating of the samples with $x=0.5$ and 0.75 under an argon flow showed no phase transition until the temperature of 1140 or 1131 K, respectively, at which peritectic decomposition occurs. Heating of the samples in air showed no oxidation below the peritectic temperature.

Phase composition of the obtained crystals was checked using powder diffraction technique. Since no peak splitting was observed and all X-ray diffraction patterns concurred with FeGa₃ we confirmed the formation of the target solid solution. The dependence of the Fe_{1–x}Co_xGa₃ unit cell volume upon the cobalt content is given in Fig. 2. Given the low values of the estimated standard deviations, the data plot presented in Fig. 2 is nonlinear showing positive and negative deviations from the Vegard’s law. In as much as the experimental dependence of unit cell volume on the number of cobalt atoms per formula unit is of great importance for understanding details of the target solid solution crystal structure, we checked whether the composition of the samples coincided with the nominal composition. For that EDX spectroscopy was used and in all cases we observed very good correspondence of the starting and actual elemental composition of the crystals. The results of the EDXS measurements as well as the calculated unit cell parameters and volume for the Fe_{1–x}Co_xGa₃ samples are summarized in Table 4.

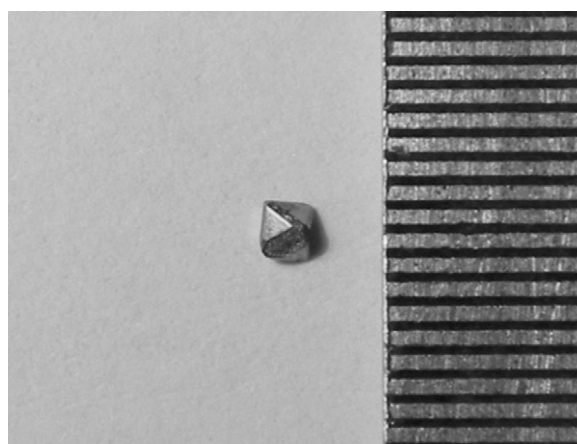


Fig. 1. Optical micrograph (background mesh size 0.5 mm) of the Fe_{0.75}Co_{0.25}Ga₃ crystal grown from Ga flux.

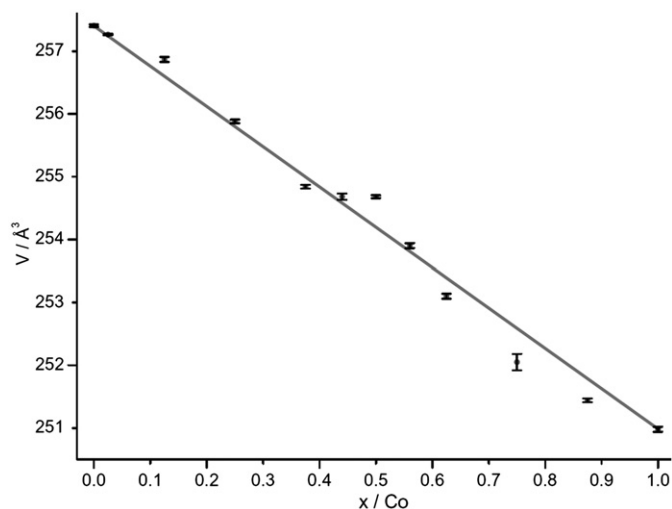


Fig. 2. Dependence of the $\text{Fe}_{1-x}\text{Co}_x\text{Ga}_3$ unit cell volume on the nominal cobalt content. Esd's are marked with black solid error bars. Solid line shows a linear dependence corresponding to the Vegard's law. (For interpretation of the references to color in this figure legend, the reader is referred to the web version of this article.)

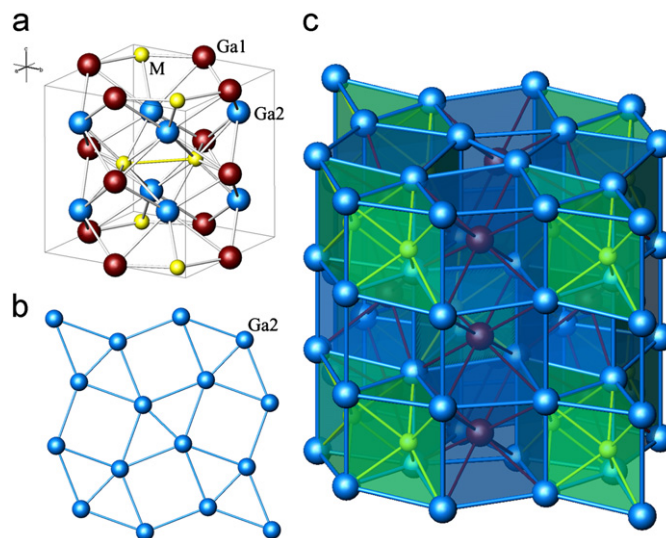


Fig. 3. Crystal structure of $\text{Fe}_{1-x}\text{Co}_x\text{Ga}_3$. (a) a view of the unit cell, (b) a $3^2 434$ net formed by the Ga2 atoms, (c) polyhedral presentation (For interpretation of the references to color in this figure legend, the reader is referred to the web version of this article.)

Table 4
Composition and unit cell parameters for $\text{Fe}_{1-x}\text{Co}_x\text{Ga}_3$.

Nominal composition [x]	Composition according to EDXS	a [Å]	c [Å]	V [Å ³]
0		6.2654 (3)	6.5572 (5)	257.41 (2)
0.025	$\text{Fe}_{0.97(1)}\text{Co}_{0.03(1)}\text{Ga}_{2.99(1)}$	6.2646 (1)	6.5553 (3)	257.27 (1)
0.125	$\text{Fe}_{0.86(5)}\text{Co}_{0.13(4)}\text{Ga}_{3.01(8)}$	6.2649 (7)	6.545 (1)	256.87 (4)
0.25	$\text{Fe}_{0.77(2)}\text{Co}_{0.26(1)}\text{Ga}_{2.97(3)}$	6.2611 (5)	6.527 (1)	255.88 (3)
0.375	$\text{Fe}_{0.62(12)}\text{Co}_{0.40(8)}\text{Ga}_{2.98(9)}$	6.2585 (4)	6.5063 (8)	254.84 (3)
0.44	$\text{Fe}_{0.57(6)}\text{Co}_{0.44(4)}\text{Ga}_{2.99(7)}$	6.2578 (6)	6.504 (1)	254.68 (5)
0.5	$\text{Fe}_{0.51(4)}\text{Co}_{0.51(8)}\text{Ga}_{2.98(8)}$	6.2594 (3)	6.5002 (3)	254.68 (2)
0.56	$\text{Fe}_{0.45(4)}\text{Co}_{0.57(4)}\text{Ga}_{2.98(5)}$	6.2553 (5)	6.489 (1)	253.90 (4)
0.625	$\text{Fe}_{0.41(4)}\text{Co}_{0.63(6)}\text{Ga}_{2.96(8)}$	6.2533 (6)	6.473 (1)	253.10 (4)
0.75	$\text{Fe}_{0.22(5)}\text{Co}_{0.80(5)}\text{Ga}_{2.98(2)}$	6.247 (1)	6.460 (2)	252.1 (1)
0.875	$\text{Fe}_{0.12(2)}\text{Co}_{0.87(9)}\text{Ga}_{3.01(9)}$	6.2431 (4)	6.4510 (9)	251.44 (3)
1		6.2421 (6)	6.441 (1)	250.98 (4)

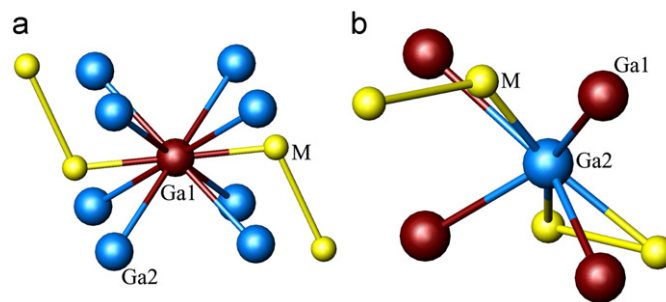


Fig. 4. Environment of the Ga1 (a) and Ga2 (b) atoms. The M atoms are shown combined into dumbbells to underline the dumbbell's orientation in the crystal structure (For interpretation of the references to color in this figure legend, the reader is referred to the web version of this article.)

3.2. Crystal structure description

Since no deviations of the elemental composition were found for the $\text{Fe}_{1-x}\text{Co}_x\text{Ga}_3$ specimens, alterations of the unit cell volume should be strongly connected to the details of crystal structure such as interatomic distances and valence angles. To investigate these details and obtain precise atomic parameters we performed structure refinement from the single-crystal X-ray diffraction data for $\text{Fe}_{0.5}\text{Co}_{0.5}\text{Ga}_3$.

A view of the crystal structure of $\text{Fe}_{0.5}\text{Co}_{0.5}\text{Ga}_3$ is presented in Fig. 3. It consists of slightly distorted $3^2 434$ nets formed by the Ga2 atoms. These nets alternate along the *c* direction and form two types of polyhedra: distorted cubes and trigonal prisms. All cubes are centered by the Ga1 atoms, while a half of the trigonal prisms are occupied by the *d* metal atoms. The assembly of the trigonal prisms is arranged in compliance with the four-fold screw axis such that the pairs of the filled and void prisms alternate in a staggered order. The crystal structure has a special feature: the M atoms are surrounded by eight Ga atoms in the form of a bicapped trigonal prism, and one M–M bond forms as a consequence of the condensation of two MGa_8 prisms via a common rectangular face. Thus there are no isolated M atoms in the structure, but only their pairs. The M–M distance of 2.7 Å

indicates weak but noticeable interactions, the nearest-neighbor distances in the respective elemental structures being 2.48 Å for *bcc*-Fe and 2.50 Å for *hcp*-Co. Accordingly, one can suppose that the nonlinear behavior of the unit cell volume versus *x* dependence could be connected to the formation of preferred pairs of *d* metals, that is, Co–Co, Fe–Fe, or Fe–Co for different values of *x*.

The Ga1 and Ga2 atoms have more complicated atomic environment presented in Fig. 4. The Ga1 atoms are surrounded by eight Ga2 atoms and two M atoms in the form of a bicapped distorted cube, whereas the Ga2 atoms have four Ga1 atoms and three M atoms in the first coordination sphere. Partial substitution of Fe by Co influences the interatomic distances, as shown in Table 3. FeGa_3 has a larger unit cell volume compared to CoGa_3 , and the interatomic distances tend to decrease from the crystal structure of FeGa_3 to that of CoGa_3 . However, most interatomic distances in $\text{Fe}_{0.5}\text{Co}_{0.5}\text{Ga}_3$ do not lie halfway between the corresponding values for binary parent compounds but lie closer to those in CoGa_3 . Moreover, one of the Ga1–Ga2 distances increases upon going from FeGa_3 to CoGa_3 . Clearly, these observations are connected to the nonlinear dependence of the unit cell volume upon the Co contents; further explanation can be obtained from the analysis of the NQR data (see below).

3.3. Electronic structure and properties

Structure optimization calculations performed first for FeGa₃ and CoGa₃ (Table 5) show excellent agreement between the experimental and calculated unit cell parameters and atomic coordinates for FeGa₃ and very good agreement for CoGa₃. This gives us possibility to achieve valid results for the intermediate compositions with the Co contents $x=0.25, 0.5,$ and 0.75 (see Supplementary Data for a complete set of symmetry information,

Table 5

Calculated with Wien2k and experimentally observed structural parameters for FeGa₃ and CoGa₃.

	FeGa ₃		CoGa ₃	
	Calculated	Experiment [4]	Calculated	Experiment [8]
<i>a</i> [Å]	6.269	6.263	6.255	6.230
<i>c</i> [Å]	6.565	6.554	6.472	6.431
<i>x</i> [M]	0.3437	0.3437	0.3451	0.3462
<i>x</i> [Ga2]	0.1557	0.1556	0.1524	0.1520
<i>z</i> [Ga2]	0.2629	0.2620	0.2566	0.2546

optimized unit cell parameters and normalized unit cell volume for the calculated structures). It should be noted that two models for $x=0.5$ were introduced, one with homoatomic Fe–Fe and Co–Co bonds and another one with only Fe–Co bonds. These two structures were calculated with more accurate parameters and showed the energy difference of $\Delta E=0.016$ eV, which is below the error of energy calculation.

The analysis of the DOS plots (Fig. 5) shows that the band structures calculated in this work for two binary compounds using the Wien2k package do not differ from those calculated previously [4,13] with the use of the programs VASP and CASTEP. There is a band gap separating the bonding states, resulted from heavy hybridization of the *d*(M) and *p*(Ga) atomic orbitals, and the predominantly nonbonding states. In FeGa₃, the Fermi level falls in the band gap of about 0.4 eV, indicating the semiconducting character. The width of the band gap is consistent with the experimental observations, which report the band gap of 0.14–0.45 eV depending on the type of measurements [14,15]. In CoGa₃, the Fermi level shifts to higher energies, above the band gap. It is located in a small pseudo gap between the predominantly nonbonding and antibonding states, making the compound metallic. The difference in properties reflects that CoGa₃ is

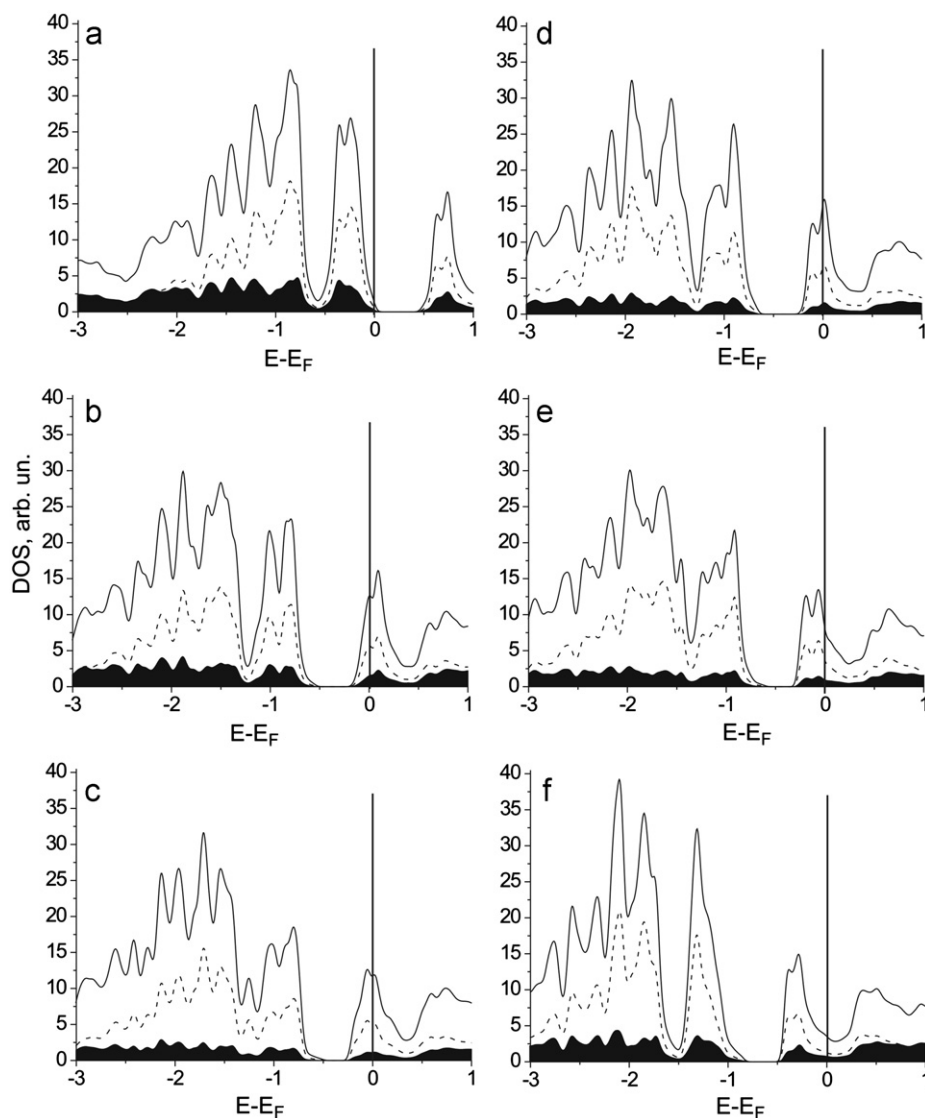


Fig. 5. Smoothed DOS plots for FeGa₃ (a), Fe_{0.75}Co_{0.25}Ga₃ (b), Fe_{0.5}Co_{0.5}Ga₃ with homoatomic dumbbells (c), Fe_{0.5}Co_{0.5}Ga₃ with heteroatomic dumbbells (d), Fe_{0.25}Co_{0.75}Ga₃ (e), and CoGa₃ (f). Total DOS, solid curves; contribution of Fe/Co d-orbitals, dashed curves; Ga contribution, shaded areas; Fermi level is marked by a vertical line.

an $18e^-$ compound, whereas FeGa_3 has one electron less. Literature data show that the isostructural compounds FeGa_3 , RuGa_3 , RuIn_3 , and OsGa_3 with $\text{VEC}=17$ are semiconductors, whereas compounds with one electron more, such as CoGa_3 , CoIn_3 or RhIn_3 , are metals [4,13,16].

The band structures of the mixed Fe/Co compounds are qualitatively the same in terms of existence of the band gap and atomic orbital contributions. The principal difference between them is the location of the Fermi level, which crosses the peaks at different positions within the region of nonbonding states (Fig. 5). Importantly, this gives rise to a different density of electronic states at the Fermi level, which can be probed with the NQR spectroscopy.

The results of the calculations are corroborated by the experimentally observed temperature dependence of the electrical resistivity for several samples with different Co concentration x (Fig. 6). The samples with x lying between 0.125 and 0.75 behave as metals. They all display relatively low electrical resistivity that increases nonlinearly with temperature up to 1–1.5 m Ω cm at 300 K. Those with $x=0.5$ –0.75 show very similar temperature dependence of the electrical resistivity with a very low increase upon increasing temperature, to a large extent resembling the properties previously reported for CoGa_3 [11]. For $x=0.125$ the resistivity drops to about 30% of its initial value from 300 to 4.2 K. The sample with $x=0.025$ behaves differently. Its resistivity is about three times higher at 300 K than for other samples, varies only slightly with temperature, and features a shallow minimum near 105 K; there is a striking resemblance of the properties of $\text{Fe}_{0.975}\text{Co}_{0.025}\text{Ga}_3$ and $\text{Fe}_{0.95}\text{Co}_{0.05}\text{Ga}_3$, the latter displaying features of a heavy-fermion metal [7]. Therefore even for $x=0.025$ semiconducting behavior is not observed. It should be noted that in isostructural $\text{RuIn}_{3-x}\text{Sn}_x$ substitution of tin for indium in the anionic substructure leads to the increase in VEC and a concomitant change from semiconducting to metallic behavior already for $x=0.01$ [17].

The results of the ab-initio electronic structure calculations also provide an initial estimation of the values of the electric field gradient (EFG) and the asymmetry parameter η which characterizes deviation of the local symmetry of the nuclei from axial (See Supplementary Data). Despite some difference, they clearly show that the gradient is the lowest for the transition metal and the highest for the Ga1 atom. Not only the values of EFG for both types of gallium atoms are different, but the most striking difference between them is provided by the η value, which points on the high asymmetry of the Ga2 environment.

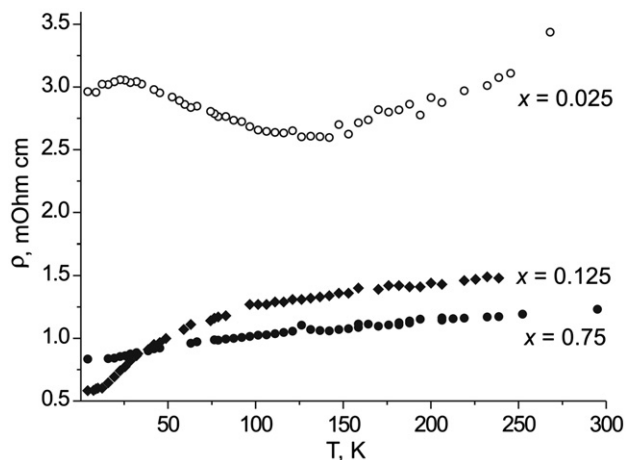


Fig. 6. Temperature dependence of electrical resistivity for selected samples of $\text{Fe}_{1-x}\text{Co}_x\text{Ga}_3$. Note that the resistivity data for $x=0.5$, 0.625 and 0.75 flow together and undistinguishable on the scale used.

3.4. NQR study of the local structure

The NQR study was undertaken to assess the local environment of Ga atoms, which can provide further information on the fine details on the crystal structure, as well as to gain more information on the electronic structure of the title solid solution.

The calculated values of EFG and η for the Ga1 and Ga2 atomic sites were recalculated to the NQR frequencies ν_Q according to the formula:

$$\nu_Q = \frac{3e^2Qq_{zz}}{2I(2I-1)\hbar} \sqrt{1 + \frac{\eta^2}{3}} \quad (1)$$

where eQ is the quadrupole moment of the ^{69}Ga (^{71}Ga) nuclei; q_{zz} is the EFG value; η is the asymmetry parameter; $I=3/2$ is the spin of the ^{69}Ga (^{71}Ga) nuclei. The obtained theoretical ν_Q values for both Ga1 and Ga2 sites for FeGa_3 and CoGa_3 compounds are listed in Table 6. As seen from this table, the theoretical ν_Q values demonstrate satisfactory coincidence with the experimental results for FeGa_3 (^{69}Ga isotope) and CoGa_3 (^{69}Ga and ^{71}Ga isotopes). Since the natural abundance of ^{69}Ga nuclei (60.4%) is significantly higher than that of ^{71}Ga nuclei (39.6%), we will consider in the following only the ^{69}Ga NQR spectra.

Experimental ^{69}Ga NQR spectra at the Ga1 and Ga2 positions for the $\text{Fe}_{1-x}\text{Co}_x\text{Ga}_3$ samples with different Co content x measured at 15 K are shown in Figs. 7 and 8, respectively. To make the spectra analysis and comparison more convenient, the frequency range in both figures is fixed at the same level of 7.5 MHz. As clearly seen from these figures, FeGa_3 and CoGa_3 compounds

Table 6
Calculated and experimental (300 K) $^{69,71}\text{Ga}$ NQR frequencies for CoGa_3 and FeGa_3 .

Compound	Ga isotope	Ga position	ν_Q calculated [MHz]	ν_Q experimental [MHz]act
CoGa_3	^{69}Ga	Ga1	33.93	35.82
		Ga2	26.77	28.45
	^{71}Ga	Ga1	21.23	22.58
		Ga2	16.75	17.94
FeGa_3	^{69}Ga	Ga1	39.91	41.25
		Ga2	33.91	34.65
	^{71}Ga	Ga1	24.58	26.00
		Ga2	20.76	21.84

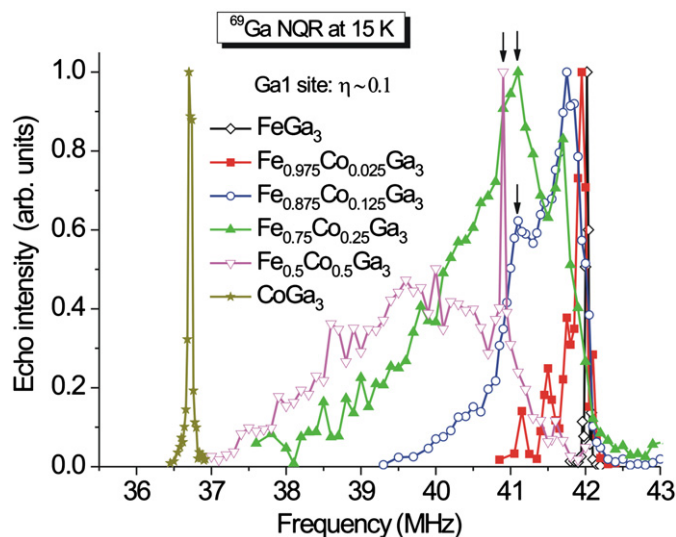


Fig. 7. Normalized ^{69}Ga NQR spectra at the Ga1 site of the $(\text{Fe}_{1-x}\text{Co}_x)\text{Ga}_3$ samples measured at 15 K (For interpretation of the references to color in this figure legend, the reader is referred to the web version of this article).

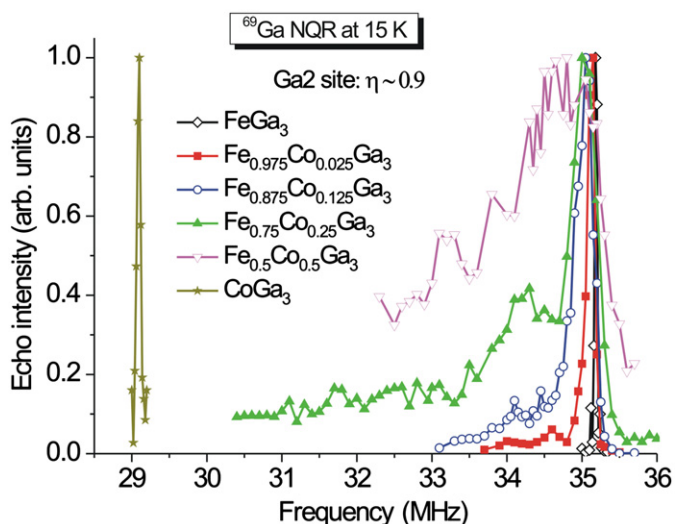


Fig. 8. Normalized ^{69}Ga NQR spectra at the Ga2 site of the $(\text{Fe}_{1-x}\text{Co}_x)\text{Ga}_3$ samples measured at 15 K. (For interpretation of the references to color in this figure legend, the reader is referred to the web version of this article.)

show very narrow sharp lines reflecting high degree of crystallographic order in the binary phases. It is worth mentioning that in CoGa_3 NQR frequencies are much less than that in FeGa_3 : by 5.32 MHz and 6.08 MHz for the Ga1 and Ga2 sites, respectively. This is a very interesting experimental observation since from the structural data (Fig. 2 and Table 4) one can expect a gradual increase of the Ga NQR frequency with increasing the Co content x in the $\text{Fe}_{1-x}\text{Co}_x\text{Ga}_3$ system due to the decrease of the unit cell volume. In general, gallium NQR frequency in the $\text{Fe}_{1-x}\text{Co}_x\text{Ga}_3$ samples can be decomposed into two terms: lattice and electronic, which stem from the influence of other ions in the lattice surrounding a given Ga site and from the charge distribution between electronic shells of a Ga atom, respectively, i.e.,

$$\nu_Q(x) = \nu_Q^{\text{latt}}(x)(1 - \gamma_\infty) + \nu_Q^{\text{el}}(x) \quad (2)$$

where γ_∞ is the Steinheimer antishielding factor, originating from the polarization of the inner electronic Ga shells caused by the charge of surrounding ions, and x is the concentration of Co. Since $\nu_Q^{\text{latt}}(x) \sim 1/V(x)$, where V is the unit cell volume, Eq. (2) can be rewritten as:

$$\nu_Q(x) = a/V(x) + \nu_Q^{\text{el}}(x) \quad (3)$$

The first term in (3) increases linearly with the Co content x because the small deviation from the Vegard's law can be neglected (see Fig. 2). Since the total experimental value $\nu_Q(x)$ goes in the opposite direction with x and is strongly suppressed with the Co substitution for Fe, we arrive at the conclusion that Ga NQR frequency in the $\text{Fe}_{1-x}\text{Co}_x\text{Ga}_3$ system is dominated by the second term in (3), i.e., by the charge redistribution between the electronic shells of Ga with increasing x .

Let us analyze in more detail the evolution of the ^{69}Ga NQR spectra with increasing the Co concentration x . We start with the Ga1 site (Fig. 7). As seen from this figure, even low Co concentration $x=0.025$ causes visible broadening of the Ga1 NQR line with a slight shift towards low frequencies and some sub-structure at the left edge. At $x=0.125$ the line broadens significantly and the pronounced peak (marked by arrow) grows up at 41.1 MHz. This peak becomes the strongest peak of the Ga1 NQR line at $x=0.25$. Finally, at $x=0.5$ we arrive at the NQR line of remarkable shape consisting of a very broad (37–42 MHz) almost symmetric hill and a sharp narrow peak (marked by an arrow) at 40.9 MHz. The

latter unambiguously evidences that notwithstanding the statistical distribution of Fe and Co atoms in the M site of the $M\text{Ga}_3$ crystal structure there exists a significant amount of Ga1 sites with exactly equivalent local surrounding in the $\text{Fe}_{0.5}\text{Co}_{0.5}\text{Ga}_3$ compound. As seen from Fig. 4(a), the only possible configuration with essential probability could be the Ga1 site with different nearest neighboring (NN) metal atoms from both sides, i.e. Fe–Ga1–Co. Indeed, in the case of the same type NN metal atoms (Fe–Ga1–Fe, or Co–Ga1–Co configurations), the local surroundings of the Ga1 site in these configurations are different, causing splitting (or broadening) of the corresponding ^{69}Ga NQR line from this Ga1 site. Considering the second metal atom in the nearest to Ga1 M–M dumbbell (see Fig. 4a), we can conclude that there are two possibilities: (i) Fe–Fe–Ga1–Co–Co (homoatomic dumbbells) and (ii) Co–Fe–Ga1–Co–Fe (heteroatomic dumbbells). Both configurations have equal probabilities in the $\text{Fe}_{0.5}\text{Co}_{0.5}\text{Ga}_3$ crystal structure and produce the narrow Ga NQR peak at 40.9 MHz.

To judge which configuration ((i) or (ii)) is realized in the $\text{Fe}_{0.5}\text{Co}_{0.5}\text{Ga}_3$ crystal structure we have to analyze the ^{69}Ga NQR spectra from the Ga2 site (Fig. 8). Again we see that the ^{69}Ga NQR line starts to broaden even at the lowest concentration of Co, $x=0.025$. But the character of the evolution of the ^{69}Ga NQR lineshape with increasing Co concentration x is different from that observed for the Ga1 site. At all x values the NQR line is broad and asymmetric without any sharp singularities. The right edge of all lines is not far from the ^{69}Ga NQR frequency of pure FeGa_3 compound. Analyzing the local surrounding of the Ga2 site (Fig. 4b) one can see that there are three metal atoms in the first coordination sphere of Ga2: the M–M dumbbell and one of M atoms from another M–M dumbbell. Therefore, the only way to obtain the observed evolution of the Ga2 NQR line with Co content x is to assume that for all $x \leq 0.5$ there is always a Fe–Fe dumbbell in vicinity of the Ga2 atom, which causes the structure of the right edge of the Ga2 NQR line. This result favors the existence of the homoatomic dumbbells Fe–Fe and Co–Co in the 50% substituted compound $\text{Fe}_{0.5}\text{Co}_{0.5}\text{Ga}_3$.

3.5. Spin–lattice relaxation

The values of the nuclear spin–lattice relaxation rate $1/T_1$ for the ^{69}Ga isotope at the Ga1 site as a function of Co concentration x at room temperature are presented in Fig. 9 (left axis). As seen from this figure, $1/T_1(x)$ has a smallest value of 1.5 s^{-1} for FeGa_3 ($x=0$) and rapidly increases with x over more than two orders of magnitude reaching the maximum value of $1.06 \times 10^3 \text{ s}^{-1}$ for $x=0.25$. With further increase of x $1/T_1(x)$ gradually decreases

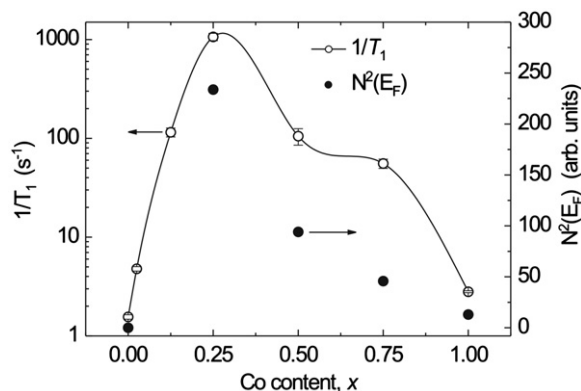


Fig. 9. Nuclear spin–lattice relaxation rate $1/T_1$ for the ^{69}Ga isotope at the Ga1 site as a function of Co concentration x at 15 K (left Y-axis). Square of the density of electronic states at the Fermi level (right Y-axis). Solid line is drawn to guide an eye.

down to the value of 2.8 s^{-1} for the binary compound CoGa_3 . This remarkable behavior correlates well with our results on the electronic structure calculations and property determination described in the previous section. Indeed, according to the DOS calculations, the $\text{Fe}_{1-x}\text{Co}_x\text{Ga}_3$ system exhibits an insulator-metal transition at Co concentration $x < 0.25$. Moreover, the metallic-like behavior in this system was observed already at very low Co concentration value of $x=0.05$ [7] and confirmed in this work for $x=0.025$. For metals the most important nuclear spin–lattice relaxation mechanism is the Korringa relaxation which represents nuclear relaxation originating from the contact interaction with conduction electrons and is given by [18]

$$(T_1^{-1})_K = \pi \hbar^3 \gamma_e^2 \gamma_n^2 A_{\text{hf}}^2 N^2(E_F) k_B T \quad (4)$$

where A_{hf} is the transferred hyperfine coupling and $N(E_F)$ is the density of electronic states (DOS) at the Fermi level. Hence, the Korringa relaxation provides an access to the hybridization-enhanced density of states at the Fermi level. As seen from Fig. 9, the square of the density of states at the Fermi level, $N^2(E_F)$, tracks the $1/T_1(x)$ behavior. Therefore, the sharp increase of $1/T_1$ at $x=0.025$ enables us to assume that the transition to the metallic state in the $\text{Fe}_{1-x}\text{Co}_x\text{Ga}_3$ system occurs already at very low Co concentration, below $x=0.025$. This result shows that the relaxation rate is very sensitive to the Co concentration and can vary within three orders of magnitude, which reflects a substantial variation of the density of electronic states. The latter value and even more the shape of the DOS curves with large slopes (Fig. 5) are responsible for large values of the Seebeck coefficient, which is proportional to the slope of the density of states near the Fermi level, $S \sim \partial N(E_F)/\partial E$ [19].

4. Conclusions

The $\text{Fe}_{1-x}\text{Co}_x\text{Ga}_3$ solid solution exists for any Co concentration and demonstrates non-Vegard behavior. Though no ordering of metal atoms was observed in its crystal structure for $x=0.5$, the analysis of the electronic structure calculated within the DFT approach and probed by $^{69,71}\text{Ga}$ NQR spectroscopy clearly shows that the metal atoms prefer to join into Fe–Fe and Co–Co dumbbells although the Fe–Co dumbbells are also present in significant amount. For $x=0.025$ the electrical resistivity is almost temperature-independent, whereas all samples with $x > 0.025$ exhibit a metallic type of the electrical conductivity, which is in line with the calculated details of the band structure. The latter shows a gap of about 0.4 eV irrespective of the Co content, however, for all compositions apart from FeGa_3 the Fermi level lies above the gap, indicating the metallic properties. For $0.25 < x < 0.75$ the Fermi level crosses peaks of high density of states. This is reflected by the rate of the nuclear spin–lattice relaxation observed in the NQR experiments, which is the highest for $x=0.25$ with the highest calculated density of electronic states at the Fermi level, $N(E_F)$,

and, in general, correlates with $N^2(E_F)$. Large values of $\partial N(E_F)/\partial E$ hint for a high Seebeck coefficient leading to appreciable thermoelectric performance, which can be tuned by varying the Co content. The study of the thermoelectric properties of $\text{Fe}_{1-x}\text{Co}_x\text{Ga}_3$ is underway.

Acknowledgments

We thank Dr. T.B. Shatalova for helping with the thermal analysis and Dr. L.I. Ryabova for fruitful discussion. This work was supported in part by the MSU priority program # 5.6 and by the Russian Foundation for Basic Research, grant # 11-08-00868-a. N.B. and W.K. were supported by the Deutsche Forschungsgemeinschaft (DFG) via TRR 80 (Augsburg-Munich).

Appendix A. Supporting information

Supplementary data associated with this article can be found in the online version at <http://dx.doi.org/10.1016/j.jssc.2012.05.041>.

References

- [1] A. Hirohata, M. Kikuchi, N. Tezuka, K. Inomata, J. Claydon, Y. Xu, G. Laan, *Curr. Opin. Solid State Mater. Sci.* 10 (2006) 93–107.
- [2] C. Felser, G. Fecher, B. Balke, *Angew. Chem. Int. Ed.* 46 (2007) 668–699.
- [3] J. Evers, G. Dehlinger, *Mat. Res. Bull.* 19 (1984) 1177–1180.
- [4] U. Häussermann, M. Boström, P. Viklund, O. Rapp, T. Björnängen, *J. Solid State Chem.* 165 (2002) 94–99.
- [5] D. Bogdanov, K. Winzer, I. Nekrasov, T. Pruschke, *J. Phys. Condens. Matter* 19 (2007) 232202.
- [6] Y. Hadano, S. Narazu, M. Avila, T. Onimaru, T. Takabatake, *J. Phys. Soc. Jpn.* 78 (2009) 013702.
- [7] E. Bittar, C. Capan, G. Seyfarth, P. Pagliuso, Z. Fisk, *J. Phys.: Conf. Ser.* 200 (2010) 012014.
- [8] A.A. Gippius, K.S. Okhotnikov, M. Baenitz, A.V. Shevelkov, *Solid State Phenom.* 152–153 (2009) 287–290.
- [9] G.M. Sheldrick, *Acta Cryst. A* 64 (2008) 112–122.
- [10] P. Blaha, K. Schwarz, G. Madsen, D. Kvasnicka, J. Luitz, WIEN2k, An Augmented Plane Wave Plus Local Orbitals Program for Calculating Crystal Properties, Vienna University of Technology, Vienna, Austria, 2001.
- [11] P. Viklund, S. Lidin, P. Berastegui, U. Häussermann, *J. Solid State Chem.* 164 (2002) 100–110.
- [12] M.G. Kanatzidis, R. Pöttgen, W. Jeitschko, *Angew. Chem. Int. Ed.* 44 (2005) 6996–7023.
- [13] Y. Imai, A. Watanabe, *Intermetallics* 14 (2006) 722–728.
- [14] N. Tsujii, H. Yamaoka, M. Matsunami, R. Eguchi, Y. Ishida, Y. Senba, H. Ohashi, S. Shin, T. Furubayashi, H. Abe, H. Kitazawa, *J. Phys. Soc. Jpn.* 77 (2008) 024705.
- [15] C.S. Lue, W.J. Lai, Y.-K. Kuo, *J. Alloys Compd.* 392 (2005) 72–75.
- [16] R. Pöttgen, R.-D. Hoffmann, G. Kotzyba, *Z. Anorg. Allg. Chem.* 624 (1998) 244–250.
- [17] M. Wagner, R. Cardoso-Gil, N. Oeschler, H. Rosner, Yu. Grin, *J. Mater. Res.* 26 (2011) 1886–1893.
- [18] C.P. Slichter, *Principles of Magnetic Resonance*, Springer, New York, 1990.
- [19] H. Kleinke, *Chem. Mater.* 22 (2010) 604–611.